

1 **Impact of stratospheric aerosol intervention geoengineering on**
2 **surface air temperature in China: A surface energy budget**
3 **perspective**

4 Zhaochen Liu^{1,3}, Xianmei Lang^{1,2}, and Dabang Jiang^{1,3*}

5 ¹Institute of Atmospheric Physics, Chinese Academy of Sciences, Beijing 100029, China

6 ²Collaborative Innovation Center on Forecast and Evaluation of Meteorological Disasters, Nanjing
7 University of Information Science and Technology, Nanjing 210044, China

8 ³College of Earth and Planetary Sciences, University of Chinese Academy of Sciences, Beijing 100049,
9 China

10 *Correspondence to:* Dabang Jiang (jiangdb@mail.iap.ac.cn)

11 **Abstract.** Stratospheric aerosol intervention (SAI) geoengineering is a proposed scheme to counteract
12 anthropogenic global warming, but the climate response to SAI, with great regional disparities, remains
13 uncertain. In this study, we use Geoengineering Model Intercomparison Project G4 experiment
14 simulations from six models that counteract anthropogenic forcing under medium-low emissions
15 (RCP4.5) by injecting a certain amount of SO₂ into the stratosphere every year, to investigate the
16 surface air temperature response to SAI geoengineering over China. We have found that SAI leads to
17 surface cooling over China during the last 40 years of injection simulation (2030–2069), which varies
18 among models, regions and seasons. Decreased tropospheric temperature and water vapor and
19 increased stratospheric aerosols induce robust decreases in downward clear-sky longwave and
20 shortwave radiation fluxes at the surface respectively, dominating the temperature change over China.
21 Changes in cloud effective forcing and surface albedo feedback also relate to the temperature response,
22 but with large spatial and seasonal variations. We find that the increased summer cloud cover and
23 winter surface albedo lead to strong cooling, while the decreased summer cloud cover and winter
24 surface albedo lead to weak cooling or even insignificant warming for the certain subregions and
25 models. Our results suggest that cloud and land surface processes in models dominate the spatial
26 pattern of SAI-induced surface air temperature change over China.

27 **1 Introduction**

28 The increasing anthropogenic greenhouse gas (GHG) concentrations since the industrial
29 revolution have led to global warming. Although the international community has realized the risk of
30 global warming and attempted to reduce GHG emissions, global GHG emissions still show a
31 continuous increase (United Nations Environment Programme, 2020). The “2°C global temperature
32 target” in the Paris Agreements will be unachievable if the current increasing emission trend persists
33 (e.g., Robiou du Pont and Meinshausen 2018). Solar radiation modification (SRM), which refers to a
34 range of measures adjusting the Earth’s radiative balance, is considered as an option to counteract
35 anthropogenic global warming. Various specific techniques have been proposed to perform SRM
36 geoengineering, such as injecting sulfate aerosols into the stratosphere (Budyko, 1977), placing shields
37 or deflectors in space (Seifritz, 1989), brightening marine clouds (Latham, 1990), and thinning cirrus
38 clouds (Mitchell and Finnegan, 2009). The method of injecting sulfate aerosols or their precursors into

39 the stratosphere, also known as stratospheric aerosol intervention (SAI) geoengineering, is designed to
40 cool the surface by using these aerosols to reflect and scatter solar radiation (Crutzen, 2006; Wigley,
41 2006). As a proposed scheme, SAI has attracted great attention recently due to its assumed
42 technological feasibility (e.g., Irvine et al., 2016).

43 SRM geoengineering has not been implemented in reality because of its potential risks and
44 immature technology. The primary means of recognizing the climate response to geoengineering is
45 simulating via general circulation models (GCMs). However, the results from early simulations could
46 not be proved robust due to the differences in experimental schemes. The Geoengineering Model
47 Intercomparison Project (GeoMIP) has been proposed to address that issue (Kravitz et al., 2011; 2015).
48 To date, the GeoMIP has designed 12 experiments, including solar dimming, stratospheric aerosol
49 intervention, marine cloud brightening, and cirrus thinning geoengineering in Coupled Model
50 Intercomparison Project Phases 5 and 6 (CMIP5 and CMIP6). The GeoMIP provides detailed
51 guidelines for each model and experiment and calls for all the modeling groups worldwide to become
52 involved and share their simulations. A total of 19 GCMs have participated in the GeoMIP to date.
53 More detailed information is accessible from the GeoMIP website
54 (<http://climate.envsci.rutgers.edu/GeoMIP/>).

55 Previous studies have indicated that SRM geoengineering could counteract or even reverse
56 anthropogenic global warming and reduce sea ice melting and thermosteric sea-level rise, as well as
57 decrease the frequency and intensity of extreme temperature and precipitation events (Rasch et al.,
58 2008; Robock et al., 2015; Irvine et al., 2016; Ji et al., 2018; Jones et al., 2018). It might also come
59 with risks. For instance, SRM geoengineering would reduce the global mean precipitation and
60 monsoon precipitation and slow the hydrological cycle if it is used to offset the GHG-induced global
61 warming (Bala et al., 2008; Tilmes et al., 2013; Sun et al., 2020). SRM would not mitigate the
62 continued ocean acidification caused by CO₂ emissions (Caldeira et al., 2013). The sudden termination
63 of geoengineering would lead to a more rapid increase in temperature than the non-geoengineered case
64 (Matthews and Caldeira, 2007; Jones et al., 2013). The severity of the termination effect depends on
65 the magnitude of geoengineering deployment. Moreover, the SAI-induced heterogeneous chemistry
66 and stratospheric circulation changes might cause stratospheric ozone depletion and thus increase
67 ultraviolet radiation (UV) at the surface (Tilmes et al., 2008, 2022; Vioni et al., 2021).

68 An appropriate SRM geoengineering strategy might lead to global cooling and benefit most

69 regions (Irvine et al., 2019). However, it was still a concern that some regions might face greater
70 climatic impacts or risks under SRM forcing (Ricke et al., 2013; Kravitz et al., 2014). For example,
71 Robock et al. (2008) indicated that the weakening of the Asian and African summer monsoons caused
72 by the injected stratospheric aerosols over the Arctic would decrease cloudiness and in turn warm the
73 surface over northern Africa and India. In addition to the effect of cloudiness, changes in atmospheric
74 moisture and surface conditions caused by SAI also impact surface air temperature (Kashimura et al.,
75 2017). As the largest developing country in the world, China plays an important role in combating
76 climate change. China’s attitude to SAI is crucial to the international geoengineering research
77 community. Considering the combined effect of the Tibetan Plateau and the East Asian monsoon, the
78 climate over China would be strongly influenced by SAI. Large volcanic eruptions, which inject
79 massive volcanic aerosols into the stratosphere, are considered a natural analog to SAI geoengineering
80 (Trenberth and Dai, 2007). The 1815 Mt. Tambora eruption led to the “year without a summer” over
81 China (e.g., Raible et al., 2016). But the volcanic eruption is not a perfect analog. This is because the
82 sulfate aerosols from massive volcanic eruptions only last for 2–3 years, while the SAI-induced
83 aerosols are continuously replenished for decades or centuries (Duan et al., 2019). So far, few studies
84 have studied the temperature response to SAI geoengineering over China explicitly (Cao et al., 2015).

85 In this study, we investigate the impact of the SAI geoengineering on the surface air temperature
86 over China and the underlying physical processes from a surface energy perspective. Section 2
87 provides a brief introduction to the experiments, model data, and decomposition method of surface air
88 temperature change. Section 3 evaluates the ability of models to reproduce the climatological
89 temperature over China in summer and winter. Section 4 presents the summer and winter temperature
90 changes and associated reasons over China in response to SAI geoengineering, and we also analyze
91 the physical processes responsible for the SAI-induced temperature changes over China. Conclusions
92 and discussion are presented in Sect. 5.

93 **2 Experiments, data, and methods**

94 **2.1 Experiments**

95 We use the G4 experiment from the first phase of the GeoMIP (Kravitz et al., 2011). As a SAI-

96 based geoengineering experiment, G4 is designed to inject SO₂ into the low-level equatorial
97 stratosphere at a consistent rate of 5 Tg per year under the background scenario of Representative
98 Concentration Pathway 4.5 (RCP4.5) (Taylor et al., 2012). This injection rate is equivalent to a case in
99 which the 1991 Mt. Pinatubo eruption occurred every four years (Bluth et al., 1992). The injection
100 period is from 2020 to 2069, and then the experiment continues to run until 2089 to examine the
101 termination effect (Jones et al., 2013). The RCP4.5 simulation for the same period is used as a baseline
102 (non-geoengineered) state. In addition, the historical simulation for 1986–2005 is applied to evaluate
103 the ability of the selected models to reproduce the climatology of surface air temperature over China.

104 **2.2 Data**

105 A total of 12 GCMs participated in the G4 experiment (Kravitz et al., 2013a). However, some
106 models should not be considered in this study due to their known issues. For instance, CSIRO-Mk3L-
107 1-2 runs G4 by directly reducing solar irradiance rather than injecting stratospheric aerosols; GISS-
108 E2-R shows an inconsistency between G4/RCP4.5 and historical experiments; IPSL-CM5A-LR and
109 NorESM1-M have errors in the longwave treatment of the sulfate aerosol; GEOSCCM and ULAQ use
110 prescribed sea surface temperatures. Simulations from the other six models are applied for analyses.
111 Monthly datasets are used and calculated as the averages in summer (June–July–August, JJA) and
112 winter (December–January–February, DJF). The CN05.1 observation dataset (Wu and Gao, 2013) is
113 used to evaluate the ability of models to reproduce the climatology of temperature over China. All the
114 observations and model outputs are interpolated to a common grid with a mid-range horizontal
115 resolution (2.5° longitude by 2° latitude).

116 A brief description of the selected models is illustrated in Table 1. In addition to differences in the
117 physical and chemical modules related to sulfate aerosol particles, the models have different SO₂
118 injection treatments. For HadGEM2-ES, the CLASSIC aerosol module (Bellouin et al., 2011) used in
119 the stratosphere makes it possible to handle the injections of SO₂, allowing HadGEM2-ES to perform
120 a complete simulation including the generation and transportation of stratospheric sulfate aerosols. The
121 injection point is located on the equator (0° longitude), and the injection altitude ranges from 16 to 25
122 km. For CanESM2, the stratospheric aerosol optical depth (SAOD) caused by SAI is prescribed as a
123 consistent value. For other models (BNU-ESM, CNRM-ESM1, MIROC-ESM and MIROC-ESM-
124 CHEM), the prescribed distribution of SAOD, according to Sato (2006), is used to drive the G4

125 experiment. Besides, MIROC-ESM-CHEM calculates the surface density of sulfate aerosols by using
 126 the CHASER atmospheric chemistry module (Sudo et al., 2002; Kravitz et al., 2013a).

127 **2.3 Decomposition method for SAI-induced surface air temperature change**

128 Surface air temperature is a widely used variable in climate studies. Change in surface air
 129 temperature is associated with three components: surface vertical energy fluxes (including radiative
 130 and heat fluxes), horizontal temperature advection, and adiabatic warming or cooling (Gong et al.,
 131 2017). In this study, the SAI-induced changes in surface temperature and surface air temperature are
 132 strongly coupled in China during 2030–2069 (the correlation coefficients are higher than 0.98 and 0.99
 133 in summer and winter, respectively; Fig. 1). Thus, the surface vertical energy fluxes are considered to
 134 be the main factor affecting temperature change under SAI forcing.

135 According to the decomposition method based on the surface energy budget proposed by Lu and
 136 Cai (2009), the surface air temperature change caused by SAI can be written as:

$$137 \quad \Delta T = \frac{\Delta R^\downarrow + \Delta LH + \Delta SH + \Delta Q}{4\sigma \overline{T_s}^3} + \text{Res} \quad (1)$$

138 where Δ represents the difference between G4 and RCP4.5, the overbar represents the climatological
 139 value of RCP4.5, R^\downarrow is the downward net radiation at the surface, LH and SH are surface sensible and
 140 latent heat fluxes respectively, Q is surface heat storage, T_s is surface temperature, and σ is the Stefan-
 141 Boltzmann constant. Res represents the difference between changes in surface air temperature and
 142 surface temperature. In order to quantitatively separate the radiative effects of clouds and surface
 143 albedo, the ΔR^\downarrow can be decomposed as follow:

$$144 \quad \Delta R^\downarrow = \Delta LW^{cs\downarrow} + (1 - \overline{\alpha}) \Delta SW^{cs\downarrow} + \Delta SAF + \Delta CRF \quad (2)$$

$$145 \quad \Delta SAF = -(\Delta SW^{as\downarrow} + \overline{SW^{as\downarrow}}) \Delta \alpha \quad (3)$$

$$146 \quad \Delta CRF = (1 - \overline{\alpha}) \Delta SW^{cl\downarrow} + \Delta LW^{cl\downarrow} \quad (4)$$

147 In Eqs. (2)–(4), $SW^{as\downarrow}$ represents downward surface shortwave radiation in all-sky conditions,
 148 $SW^{cs\downarrow}$ and $LW^{cs\downarrow}$ represent downward surface shortwave and longwave radiations in clear-sky
 149 conditions respectively, $SW^{cl\downarrow}$ and $LW^{cl\downarrow}$ represent downward shortwave and longwave radiative
 150 effects of clouds (all-sky radiations minus clear-sky radiations) respectively, and α represents surface

151 albedo (the ratio of solar radiation reflected to the atmosphere at the surface). SAF is surface albedo
 152 feedback, and CRF is cloud radiative forcing. Under SAI forcing, both the changes in atmospheric
 153 reflection and atmospheric absorption affect the $SW^{cs\downarrow}$. We assume that the clear-sky atmospheric
 154 reflection change is only affected by atmospheric water vapor amount, and the clear-sky atmospheric
 155 absorption change is only affected by the aerosol scattering effect. As detailed by Kashimura et al.
 156 (2017), the change in $SW^{cs\downarrow}$ can be further decomposed as:

$$157 \quad \Delta SW^{cs\downarrow} \approx \Delta SW_{SRM} + \Delta SW_{WV} \quad (5)$$

$$158 \quad \Delta SW_{SRM} = SW^{cs\downarrow}(F_{G4}^{cs}, A_{RCP}^{cs}) - \overline{SW^{cs\downarrow}} \quad (6)$$

$$159 \quad \Delta SW_{WV} = SW^{cs\downarrow}(F_{RCP}^{cs}, A_{G4}^{cs}) - \overline{SW^{cs\downarrow}} \quad (7)$$

160 where F is the fraction of solar radiation reflected by the atmosphere, and A is the fraction of absorption
 161 during solar radiation passing through the atmosphere. SW_{SRM} and SW_{WV} represent the effects of solar
 162 radiation scattering and atmospheric water vapor amount, respectively. Although the $SW^{cs\downarrow}$ change is
 163 not precisely equal to the sum of changes in SW_{SRM} and SW_{WV} due to the assumption of a single-layer
 164 model (Donohoe and Battisti, 2011), this method is effective when analyzing the surface shortwave
 165 radiation change in response to SAI (Kashimura et al., 2017).

166 **3 Evaluation of the models**

167 The ability of the models to reproduce the surface air temperature over China is evaluated first.
 168 As shown in Fig. 2, the spatial correlation coefficient (SCC), standard deviation (SD), and centered
 169 root-mean-square error (CRMSE) between the observation and the historical simulation for
 170 climatological temperature over China during 1986–2005 are calculated and illustrated in a Taylor
 171 diagram (Taylor, 2001). The SCCs of the models range from 0.85 to 0.95 (0.94 in multi-model mean)
 172 in summer and from 0.91 to 0.96 (0.96 in multi-model mean) in winter. All the SCCs are statistically
 173 significant at the 99% level, meaning that the simulated temperature is in good agreement with the
 174 observed temperature. The normalized SDs range from 0.81 to 1.33 in summer (0.99 in multi-model
 175 mean) and from 1.03 to 1.23 (1.08 in multi-model mean) in winter. This result indicates that all
 176 selected models overestimate the spatial variability of the winter temperature in China. The CRMSEs
 177 are 0.34–0.53 (0.35 in multi-model mean) for summer and 0.32–0.46 (0.31 in multi-model mean) for

178 winter. Taken together, the simulations of summer and winter temperatures by selected models are
179 reliable over China. The multi-model mean results outperform most individual models for the
180 temperature climatology over China both in summer and winter, which is consistent with previous
181 findings (e.g., Jiang et al., 2016).

182 The observed spatial patterns of summer and winter temperature climatology over China show
183 a general decrease from south to north, and the lowest values mainly occur in the Tibetan Plateau
184 (Figs. 3a, d). These features can be well reproduced by all models and their mean (Figs. 3b, e).
185 Compared to the observation, the simulated temperature is generally overestimated in summer but
186 underestimated in winter over China according to the regionally averaged values. In summer, warm
187 biases occur in most of eastern China, especially in northeastern China (Fig. 3c). In winter, however,
188 the underestimation of temperature exists at the national scale, with a regionally averaged cold bias
189 of 1.79°C in multi-model mean (Fig. 3f). Substantial cold biases occur over the Tarim Basin and the
190 Tibetan Plateau, which are associated with regional topography. Most of the above biases are
191 consistent among individual models, with the averaged model consistency of 76% over China in both
192 summer and winter.

193 **4 Results**

194 **4.1 Changes in surface air temperature over China**

195 Figures 4 and 5 show the temporal evolution of surface air temperature changes in the G4
196 experiment and RCP4.5 scenario relative to the present climatology (1986–2005) over China. Both the
197 summer and winter temperatures in G4 increase over time, although they are colder than those in
198 RCP4.5. Positive values occur throughout the whole G4 simulation period, excluding several years in
199 winter. This indicates that although the injection of 5 Tg SO₂ per year leads to a surface cooling over
200 China, the climatological temperature in G4 is still higher than the present level. Considering that the
201 feedback response timescale of diffusive ocean heat uptake in climate models is approximately ten
202 years (Jarvis, 2011), the simulation representing the last 40 years of injection (2030–2069) is used to
203 examine the temperature response to SAI over China, as done by Kravitz et al. (2013b) and Tilmes et
204 al. (2013). During this period, the warming trends over all of China in G4 among models are 0.21–

205 0.43°C decade⁻¹ in summer and 0.30–0.59°C decade⁻¹ in winter. It can be seen that the warming trend
206 difference between G4 and RCP4.5 is small, and this is expected because of the similar trend of
207 radiative forcing variation in the two experiments during 2030–2069. The regionally averaged
208 temperature over China is decreased by 0.24–0.96°C (0.64°C in the multi-model mean) in summer and
209 0.30–1.52°C (0.80°C in the multi-model mean) in winter due to SAI forcing. Although the magnitude
210 of SAI-induced temperature change varies across models and seasons, the cooling response is
211 consistent among models over China. The winter cooling is stronger than the summer level in all
212 models. Additionally, the result shows the strongest SAI-induced cooling occurs in HadGEM2-ES in
213 both summer and winter.

214 The spatial pattern of the temperature difference between G4 and RCP4.5 over China is illustrated
215 in Figs. 6 and 7. The multi-model results show a robust and coherent cooling in both summer and
216 winter. Strong cooling with magnitudes greater than 0.8°C mainly occurs over high-latitude regions,
217 including northwestern and central China. For the individual models, the SAI-induced temperature
218 changes are negative and significant almost everywhere over China except for in MIROC-ESM and
219 MIROC-ESM-CHEM. SAI leads to the temperature increases over the upper reaches of the Yellow
220 River and the middle and upper reaches of the Yangtze River in MIROC-ESM in winter, and over
221 northeastern and southeastern China in MIROC-ESM-CHEM in summer, respectively (Figs. 6f and
222 7e). These increases are weak and insignificant. The physical processes responsible for SAI-induced
223 cooling or warming will be discussed in the subsequent sections.

224 4.2 Decomposition of SAI-induced temperature change

225 We decompose the SAI-induced change in surface air temperature over China by utilizing Eqs.
226 (1)–(4). The regionally averaged value of each term is illustrated in Fig. 8. It can be seen that SAI
227 decreases downward net surface radiation fluxes, leading to a surface cooling of 0.30–1.45°C in
228 summer and 0.48–2.10°C in winter over China. These decreases are partly compensated by decreased
229 nonradiative fluxes, especially the decreased LH. The contributions of SH, Q , and Res are relatively
230 small (Fig. 8a). The decomposition of downward surface radiation shows the decreases in $SW^{cs\downarrow}$ and
231 $LW^{cs\downarrow}$ in all models. The reduced $LW^{cs\downarrow}$ dominates the deficient downward net surface radiation and
232 decreases the temperature with magnitudes of 0.38–1.33°C in summer and 0.25–1.38°C in winter. The
233 reduced $SW^{cs\downarrow}$ also contributes to the surface cooling, with magnitudes of 0.04–0.33°C in summer and

234 0.13–0.41°C in winter. The winter decrease in $SW^{cs\downarrow}$ is stronger than the summer one in most models.
235 Besides, the inter-model differences in CRF and SAF changes are relatively substantial. The area-
236 averaged results illustrate that the changes in CRF and SAF have negative and positive contributions
237 to the SAI-induced cooling over China in most models, respectively (Fig. 8b).

238 The spatial patterns of SAI-induced changes in key energy-related variables over China are
239 illustrated in Fig. 9. Under SAI forcing, changes in atmospheric temperature and water vapor lead to a
240 general decrease in the $LW^{cs\downarrow}$. The $SW^{cs\downarrow}$, primarily related to the solar radiation scattering effect by
241 stratospheric sulfate aerosol particles, also exhibits a coherent reduction over China. The spatial pattern
242 of temperature change over China is primarily determined by $SW^{cl\downarrow}$ and surface albedo changes. In
243 summer, most models exhibit increases in cloud amount, especially over northwestern and central
244 China. The resultant decreased $SW^{cl\downarrow}$ leads to strong cooling over these regions. Conversely,
245 northeastern and southeastern China show increased $SW^{cl\downarrow}$ and relatively weak cooling (Fig. 9d). In
246 MIROC-ESM-CHEM, the excessive $SW^{cl\downarrow}$ (up to 8 W m^{-2}) offsets the clear-sky radiative effects and
247 causes abnormal warming over most regions of eastern China (Fig. S1a). In summer, the surface albedo
248 change due to SAI over China is relatively small. The increased surface albedo mainly occurs in the
249 Tibetan Plateau, which contributes to local surface cooling (Fig. 9f). This may help to explain why the
250 cloud effect is not a primary factor of temperature change over the Tibetan Plateau in summer.

251 In winter, a robust and coherent SAI-induced reduction in cloud cover is found over China (Fig.
252 9k). This reduction leads to a general increase in $SW^{cl\downarrow}$, causing the weak cooling south of the Yangtze
253 River valley. In other areas of China, however, the change in surface albedo is the primary factor
254 affecting the spatial pattern of temperature response under SAI forcing. The increased surface albedo
255 leads to strong cooling, especially over northwestern and central China. However, the decreased
256 surface albedo is found over the upper reaches of the Yellow River and the middle and upper reaches
257 of the Yangtze River in MIROC-ESM with magnitudes greater than 3%, which results in the abnormal
258 winter warming mentioned above (Fig. S1d). Taken together, the increased summer cloud cover and
259 winter surface albedo lead to strong cooling, while the decreased summer cloud cover and winter
260 surface albedo result in weak cooling, or even warming for the certain subregions and models, for
261 instance eastern China in MIROC-ESM-CHEM and the upper reaches of the Yellow River and the
262 middle and upper reaches of the Yangtze River in MIROC-ESM.

263 4.3 Physical processes responsible for SAI-induced temperature changes

264 Previous studies have illustrated that the SAI reduces the tropospheric temperature and
265 atmospheric water vapor amount on a global scale (Kashimura et al., 2017; Vioni et al., 2018). In
266 China, these reductions cause the decreased $LW^{cs\downarrow}$, contributing to the surface cooling primarily. We
267 further address the potential reasons for the $SW^{cs\downarrow}$ change by using the aforementioned decomposition
268 method. The atmospheric reflection of solar radiation increases after sulfate aerosols injection. In our
269 study, the effect of aerosols scattering on shortwave radiation is represented as SW_{SRM} , which can be
270 measured by the change in SAOD. As shown in Fig. 10, the latitudinal distributions of the calculated
271 (used in HadGEM2-ES) and prescribed (used in BNU-ESM, CNRM-ESM1 and the MIROC-based
272 models) SAOD changes caused by SAI in G4 display a coherent increase over China. The distribution
273 in CanESM2 is not shown because it is a constant field according to the experimental design. The
274 SAOD change in HadGEM2-ES is unavailable. Total aerosol optical depth is therefore considered as
275 a reasonable alternative variable for SAOD (e.g., Bellouin et al., 2011). The national-scale increased
276 SAOD results in a robust decrease in SW_{SRM} (Figs. 11a, d), contributing to the surface cooling with
277 magnitudes of 0.21–0.54°C in summer and 0.26–0.69°C in winter. Besides, the deficit in column-
278 integrated water vapor reduces the atmospheric absorption of solar radiation. The resultant increased
279 SW (SW_{wv}) counterbalance 37–81% and 11–48% of the reductions in SW_{SRM} over China in summer
280 and winter, respectively (Figs. 11b, e). This is the main reason why the SAI-induced winter cooling is
281 severer than the summer level.

282 As discussed in Sect. 4.2, the spatial patterns of summer and winter temperature changes over
283 China are mainly determined by the $SW^{cl\downarrow}$ and surface albedo, respectively. Generally, the SAI-induced
284 decrease in LH flux reduces the low cloud cover, resulting in the positive change in $SW^{cl\downarrow}$ (Figs. 11c,
285 f). Through this process, the significantly decreased LH over northeastern and southeastern China
286 causes the abnormal summer warming in MIROC-ESM-CHEM (Fig. S1c). However, in summer, the
287 effect of LH is partly offset by the SAI-induced moisture convergence at the troposphere in most
288 models. The resultant increased cloud cover enhances the surface cooling over northwestern and
289 central China (Fig. 11h). The change in surface albedo is closely related to land surface conditions.
290 The SAI-induced cooling can be amplified by increased snow cover or sea ice (e.g., Schmidt et al.,
291 2012). Considering surface albedo can be reasonably described as a linear function of snow cover

292 fraction (Qu and Hall, 2007; Li et al., 2016), we further investigate the spatial pattern of changes in
293 snow cover fraction, and find that matches with surface albedo over China (Figs. 11i, l; note that model
294 data are not available for HadGEM2-ES). Under SAI forcing, the increased snow cover mainly occurs
295 over the Tibetan Plateau in summer, and over northwestern and central China in winter. The enlarged
296 snow cover fraction gives rise to SW decrease at the surface, which in turn has a positive feedback on
297 surface cooling. Furthermore, the SAI-induced abnormal winter warming in MIROC-ESM is also
298 associated with the decreased snow cover over the upper reaches of the Yellow River and the middle
299 and upper reaches of the Yangtze River (Fig. S1e).

300 **5 Conclusions and discussion**

301 We analyze the surface air temperature response to SAI forcing over China based on the
302 simulations of the G4 experiment and RCP4.5 scenario by using six GCMs (BNU-ESM, CanESM2,
303 CNRM-ESM1, HadGEM2-ES, MIROC-ESM and MIROC-ESM-CHEM). We also discuss the
304 physical processes involved in the temperature response from a surface energy budget perspective. The
305 main conclusions are summarized as follows.

306 (1) All selected models can well reproduce the present climatological surface air temperature over
307 China in both summer and winter. Although the SAI in the G4 experiment leads to a surface cooling
308 over China, the climatological temperature in G4 is still higher than the present level. During the
309 simulation period of 2030–2069, SAI leads to a national-scale cooling over China in all models.
310 Regionally, the multi-model mean cooling is 0.64°C in summer and 0.80°C in winter, respectively. The
311 SAI-induced temperature change varies among models, regions and seasons.

312 (2) The decomposition of temperature change based on the surface energy budget indicates that
313 the SAI-induced surface cooling over China is dominated by the robust decrease in downward clear-
314 sky radiation fluxes (particularly in downward clear-sky longwave radiation flux), and associated with
315 the changes in cloud effective forcing and surface albedo feedback. The shortwave radiative effect of
316 clouds and the surface albedo feedback determine the spatial pattern of temperature change, which are
317 somewhat model-dependent and display a level of regional and seasonal discrepancies.

318 (3) Under SAI forcing, the decreased downward clear-sky longwave radiation is mainly due to
319 the decreased tropospheric temperature and water vapor amount, and the decreased downward clear-

320 sky shortwave radiation is mainly contributed by the aerosol scattering effect over China. The
321 decreased latent heat flux generally reduces the cloud cover over China, but the change in summer
322 cloud cover is closely associated with the anomalous tropospheric moisture flux convergence. The
323 negative surface albedo feedback related to increased snow cover fraction also amplifies the surface
324 cooling, especially over the Tibetan Plateau in summer, and over northwestern and central China in
325 winter. The results above are summarized schematically in Fig. 12.

326 Finally, equatorial stratospheric SO₂ injection has been proposed as a convenient and efficient
327 strategy of SAI geoengineering because the large-scale atmospheric circulation can transport sulfate
328 aerosols around the globe automatically. But it leads to regional inequities in the temperature response
329 due to the strong confinement of the Brewer-Dobson circulation (Kravitz et al., 2016). This means that
330 some areas will face more severe climatic disasters if this kind of geoengineering is implemented. To
331 solve this issue, certain SAI experiments based on the injection at multiple locations have been
332 proposed, such as the stratospheric aerosol geoengineering large ensemble project (GLENS) using
333 CESM1(WACCM) (Tilmes et al., 2018; Kravitz et al., 2019). In addition, the uncertainty of the
334 regional climate response to SAI is closely related to the reliability of the models (Irvine et al., 2016).
335 It has been indicated that the CMIP6 GCMs perform better in simulating the temperature over China
336 than their CMIP5 counterparts (Jiang et al., 2020). Therefore, the climate response to SAI
337 geoengineering over China based on state-of-the-art GCM experiments merits further study.

338 *Code and data availability.* The dataset used in this study can be accessed with the following links:
339 <https://esgf-node.llnl.gov/search/cmip5/>.

340 *Author contributions.* Dabang Jiang and Zhaochen Liu designed and performed the research. Zhaochen
341 Liu and Xianmei Lang analyzed the data. Zhaochen Liu and Dabang Jiang wrote the manuscript. All
342 authors contributed to this study.

343 *Competing interests.* The authors declare no competing interests.

344 *Acknowledgments.* We sincerely thank the four anonymous reviewers for their insightful comments

345 and suggestions to improve this manuscript. We acknowledge the Geoengineering Model
346 Intercomparison Project Steering Committee and the World Climate Research Program's Working
347 Group on Coupled Modelling. We also thank the climate modelling groups for producing their model
348 outputs. We thank Helene Muri, Ji Duoying, John Moore and Toshihiro Nemoto for their help in
349 downloading the GeoMIP outputs. This work was supported by the National Natural Science
350 Foundation of China (42175031 and 41991284).

351 **References**

- 352 Arora, V. K., Scinocca, J. F., Boer, G. J., Christian, J. R., Denman, K. L., Flato, G. M., Kharin, V. V.,
353 Lee, W. G., and Merryfield, W. J.: Carbon emission limits required to satisfy future representative
354 concentration pathways of greenhouse gases, *Geophys. Res. Lett.*, 38, L05805,
355 <https://doi.org/10.1029/2010GL046270>, 2011.
- 356 Bala, G., Duffy, P. B., and Taylor, K. E.: Impact of geoengineering schemes on the global hydrological
357 cycle, *Proc. Natl. Acad. Sci. U. S. A.*, 105, 7664–7669, <https://doi.org/10.1073/pnas.0711648105>,
358 2008.
- 359 Bellouin, N., Rae, J., Jones, A., Johnson, C., Haywood, J., and Boucher, O.: Aerosol forcing in the
360 Climate Model Intercomparison Project (CMIP5) simulations by HadGEM2-ES and the role of
361 ammonium nitrate, *J. Geophys. Res.*, 116, D20206, <https://doi.org/10.1029/2011JD016074>, 2011.
- 362 Bluth, G. J., Doiron, S. D., Schnetzler, C. C., Krueger, A. J., and Walter, L. S.: Global tracking of the
363 SO₂ clouds from the June, 1991 Mount Pinatubo eruptions, *Geophys. Res. Lett.*, 19, 151–154,
364 <https://doi.org/10.1029/91GL02792>, 1992.
- 365 Budyko, M. I.: *Climatic Changes*, American Geophysical Union, Washington, DC, 244 pp.,
366 <https://doi.org/10.1029/SP010>, 1977.
- 367 Caldeira, K., Bala, G., and Cao, L.: The science of geoengineering. *Annu. Rev. Earth Planet. Sci.*, 41,
368 231–256, <https://doi.org/10.1146/annurev-earth-042711-105548>, 2013.
- 369 Cao, L., Gao, C. C., and Zhao, L. Y.: Geoengineering: Basic science and ongoing research efforts in
370 China, *Adv. Clim. Chang. Res.*, 6, 188–196, <http://dx.doi.org/10.1016/j.accre.2015.11.002>, 2015.
- 371 Collins, W. J., Bellouin, N., Doutriaux-Boucher, M., Gedney, N., Halloran, P., Hinton, T., Hughes, J.,
372 Jones, C. D., Joshi, M., Liddicoat, S., Martin, G., O'Connor, F., Rae, J., Senior, C., Sitch, S.,

373 Totterdell, I., Wiltshire, A., and Woodward, S.: Development and evaluation of an earth-system
374 model – HadGEM2, *Geosci. Model Dev.*, 4, 1051–1075, [https://doi.org/10.5194/gmd-4-1051-](https://doi.org/10.5194/gmd-4-1051-2011)
375 2011, 2011.

376 Crutzen, P. J.: Albedo enhancement by stratospheric sulfur injections: A contribution to resolve a policy
377 dilemma? *Clim. Change*, 77, 211–220, <https://doi.org/10.1007/s10584-006-9101-y>, 2006.

378 Duan, L., Cao, L., Bala, G., and Caldeira, K.: Climate response to pulse versus sustained stratospheric
379 aerosol forcing, *Geophys. Res. Lett.*, 46, 8976–8984, <https://doi.org/10.1029/2019GL083701>,
380 2019.

381 Donohoe, A., and Battisti, D. S.: Atmospheric and surface contributions to planetary albedo, *J. Clim.*,
382 24, 4402–4418, <https://doi.org/10.1175/2011JCLI3946.1>, 2011.

383 Gong, T., Feldstein, S., and Lee, S.: The role of downward infrared radiation in the recent Arctic winter
384 warming trend, *J. Clim.*, 30, 4937–4949, <https://doi.org/10.1175/JCLI-D-16-0180.1>, 2017.

385 Irvine, P. J., Kravitz, B., Lawrence, M. G., and Muri, H.: An overview of the Earth system science of
386 solar geoengineering, *Wiley Interdiscip. Rev.-Clim. Chang.*, 7, 815–833,
387 <https://doi.org/10.1002/wcc.423>, 2016.

388 Irvine, P. J., Emanuel, K., He, J., Horowitz, L. W., Vecchi, G., and Keith, D.: Halving warming with
389 idealized solar geoengineering moderates key climate hazards, *Nat. Clim. Change*, 9, 295–299,
390 2019.

391 Jarvis, A.: The magnitudes and timescales of global mean surface temperature feedbacks in climate
392 models, *Earth Syst. Dynam.*, 2, 213–221, <https://doi.org/10.5194/esd-2-213-2011>, 2011.

393 Ji, D., Wang, L., Feng, J., Wu, Q., Cheng, H., Zhang, Q., Yang, J., Dong, W., Dai, Y., Gong, D., Zhang,
394 R. H., Wang, X., Liu, J., Moore, J. C., Chen, D., and Zhou, M.: Description and basic evaluation
395 of Beijing Normal University Earth System Model (BNU-ESM) version 1, *Geosci. Model Dev.*,
396 7, 2039–2064, <https://doi.org/10.5194/gmd-7-2039-2014>, 2014.

397 Ji, D., Fang, S., Curry, C., Kashimura, H., Watanabe, S., Cole, J. N., Lenton, A., Muri, H., Kravitz, B.,
398 and Moore, J.: Extreme temperature and precipitation response to solar dimming and
399 stratospheric aerosol geoengineering, *Atmos. Chem. Phys.*, 18, 10133–10156,
400 <https://doi.org/10.5194/acp-18-10133-2018>, 2018.

401 Jiang, D., Tian, Z., and Lang, X.: Reliability of climate models for China through the IPCC third to
402 fifth assessment reports, *Int. J. Climatol.*, 36, 1114–1133, <https://doi.org/10.1002/joc.4406>, 2016.

403 Jiang, D., Hu, D., Tian, Z., and Lang, X.: Differences between CMIP6 and CMIP5 models in simulating
404 climate over China and the East Asian monsoon, *Adv. Atmos. Sci.*, 37, 1102–1118,
405 <https://doi.org/10.1007/s00376-020-2034-y>, 2020.

406 Jones, A., Haywood, J. M., Alterskjær, K., Boucher, O., Cole, J. N., Curry, S., Charles, L., Irvine, P. J.,
407 Ji, D., Kravitz, B., Egill-Kristjánsson, J., Moore, J. C., Niemeier, U., Robock, A., Schmidt, H.,
408 Singh, B., Tilmes, S., Watanabe, S., and Yoon, J.-H.: The impact of abrupt suspension of solar
409 radiation management (termination effect) in experiment G2 of the Geoengineering Model
410 Intercomparison Project (GeoMIP), *J. Geophys. Res.-Atmos.*, 118, 9743–9752,
411 <https://doi.org/10.1002/jgrd.50762>, 2013.

412 Jones, A. C., Hawcroft, M. K., Haywood, J. M., Jones, A., Guo, X., and Moore, J. C.: Regional climate
413 impacts of stabilizing global warming at 1.5 K using solar geoengineering, *Earths Future*, 6, 230–
414 251, <https://doi.org/10.1002/2017EF000720>, 2018.

415 Kashimura, H., Abe, M., Watanabe, S., Sekiya, T., Ji, D., Moore, J. C., Cole, J. N., and Kravitz, B.:
416 Shortwave radiative forcing, rapid adjustment, and feedback to the surface by sulfate
417 geoengineering: Analysis of the Geoengineering Model Intercomparison Project G4 scenario,
418 *Atmos. Chem. Phys.*, 17, 3339–3356, <https://doi.org/10.5194/acp-17-3339-2017>, 2017.

419 Kravitz, B., Robock, A., Boucher, O., Schmidt, H., Taylor, K. E., Stenchikov, G., and Schulz, M.: The
420 Geoengineering Model Intercomparison Project (GeoMIP), *Atmos. Sci. Lett.*, 12, 162–167,
421 <https://doi.org/10.1002/asl.316>, 2011.

422 Kravitz, B., Robock, A., Forster, P. M., Haywood, J. M., Lawrence, M. G., and Schmidt, H.: An
423 overview of the Geoengineering Model Intercomparison Project (GeoMIP), *J. Geophys. Res.-*
424 *Atmos.*, 118, 13103–13107, <https://doi.org/10.1002/2013JD020569>, 2013a.

425 Kravitz, B., Rasch, P. J., Forster, P. M., Andrews, T., Cole, J. N., Irvine, P. J., Ji, D., Kristjánsson, J.,
426 Moore, J. C., Muri, H., Niemeier, U., Robock, A., Singh, B., Tilmes, S., Watanabe, S., and Yoon,
427 J.-H.: An energetic perspective on hydrological cycle changes in the Geoengineering Model
428 Intercomparison Project, *J. Geophys. Res.-Atmos.*, 118, 13087–13102,
429 <https://doi.org/10.1002/2013JD020502>, 2013b.

430 Kravitz, B., MacMartin, D. G., Robock, A., Rasch, P. J., Ricke, K. L., Cole, J. N., Curry, C. L., Irvine,
431 P. J., Ji, D., Keith, D. W., Kristjánsson, J. E., Moore, J. C., Muri, H., Singh, B., Tilmes, S.,
432 Watanabe, S., Yang, S., and Yoon, J. H.: A multi-model assessment of regional climate disparities

433 caused by solar geoengineering, *Environ. Res. Lett.*, 9, 074013, <https://doi.org/10.1088/1748->
434 9326/9/7/074013, 2014.

435 Kravitz, B., Robock, A., Tilmes, S., Boucher, O., English, J. M., Irvine, P. J., Jones, A., Lawrence, M.
436 G., MacCracken, M., Muri, H., Moore, J. C., Niemeier, U., Phipps, S. J., Sillmann, J., Storelvmo,
437 T., Wang, H., and Watanabe, S.: The Geoengineering Model Intercomparison Project Phase 6
438 (GeoMIP6): simulation design and preliminary results, *Geosci. Model Dev.*, 8, 3379–3392,
439 <https://doi.org/10.5194/gmd-8-3379-2015>, 2015.

440 Kravitz, B., MacMartin, D. G., Wang, H., and Rasch, P. J.: Geoengineering as a design problem, *Earth*
441 *Syst. Dynam.*, 7, 469–497, <https://doi.org/10.5194/esd-7-469-2016>, 2016.

442 Kravitz, B., MacMartin, D. G., Tilmes, S., Richter, J. H., Mills, M. J., Cheng, W., Dagon, K., Glanville,
443 A. S., Lamarque, J.-F., Simpson, I. R., Tribbia, J., and Vitt, F.: Comparing surface and
444 stratospheric impacts of geoengineering with different SO₂ injection strategies, *J. Geophys. Res.-*
445 *Atmos.*, 124, 7900–7918, <https://doi.org/10.1029/2019JD030329>, 2019.

446 Latham, J.: Control of global warming? *Nature*, 347, 339–340, <https://doi.org/10.1038/347339b0>, 1990.

447 Li, Y., Wang, T., Zeng, Z., Peng, S., Lian, X., and Piao, S.: Evaluating biases in simulated land surface
448 albedo from CMIP5 global climate models, *J. Geophys. Res.-Atmos.*, 121, 6178–6190,
449 <https://doi.org/10.1002/2016JD024774>, 2016.

450 Lu, J., and Cai, M.: Seasonality of polar surface warming amplification in climate simulations,
451 *Geophys. Res. Lett.*, 36, L16704, <https://doi.org/10.1029/2009GL040133>, 2009.

452 Matthews, H. D., and Caldeira, K.: Transient climate–carbon simulations of planetary geoengineering,
453 *Proc. Natl. Acad. Sci. U. S. A.*, 104, 9949–9954, <https://doi.org/10.1073/pnas.0700419104>, 2007.

454 Mitchell, D. L., and Finnegan, W.: Modification of cirrus clouds to reduce global warming, *Environ.*
455 *Res. Lett.*, 4, 045102, <https://doi.org/10.1088/1748-9326/4/4/045102>, 2009.

456 Qu, X., and Hall, A.: What controls the strength of snow-albedo feedback? *J. Clim.*, 20, 3971–3981,
457 <https://doi.org/10.1175/JCLI4186.1>, 2007.

458 Raible, C. C., Brönnimann, S., Auchmann, R., Brohan, P., Frölicher, T. L., Graf, H. F., Jones, P.,
459 Luterbacher, J., Muthers, S., Neukom, R., Robock, A., Self, S., Sudrajat, A., Timmreck, C., and
460 Wegmann, M.: Tambora 1815 as a test case for high impact volcanic eruptions: Earth system
461 effects, *Wiley Interdiscip. Rev.-Clim. Chang.*, 7, 569–589, <https://doi.org/10.1002/wcc.407>, 2016.

462 Rasch, P. J., Crutzen, P. J., and Coleman, D. B.: Exploring the geoengineering of climate using

463 stratospheric sulfate aerosols: The role of particle size, *Geophys. Res. Lett.*, 35, L02809,
464 <https://doi.org/10.1029/2007GL032179>, 2008.

465 Ricke, K. L., Moreno-Cruz, J. B., and Caldeira, K.: Strategic incentives for climate geoengineering
466 coalitions to exclude broad participation, *Environ. Res. Lett.*, 8, 014021,
467 <https://doi.org/10.1088/1748-9326/8/1/014021>, 2013.

468 Robiou du Pont, Y., and Meinshausen, M.: Warming assessment of the bottom-up Paris Agreement
469 emissions pledges, *Nat. Commun.*, 9, 4810, <https://doi.org/10.1038/s41467-018-07223-9>, 2018.

470 Robock, A., Oman, L., and Stenchikov, G. L.: Regional climate responses to geoengineering with
471 tropical and Arctic SO₂ injections, *J. Geophys. Res.*, 113, D16,
472 <https://doi.org/10.1029/2008JD010050>, 2008.

473 Robock, A.: Stratospheric aerosol geoengineering, *AIP Conf. Proc.*, 1652, 183–197,
474 <https://doi.org/10.1063/1.4916181>, 2015.

475 Sato, M.: Forcings in GISS climate model: Stratospheric aerosol optical thickness, available at:
476 <https://data.giss.nasa.gov/modelforce/strataer/>, 2006. (last access: April 2021)

477 Schmidt, H., Alterskjær, K., Bou Karam, D., Boucher, O., Jones, A., Kristjánsson, J. E., Niemeier, U.,
478 Schulz, M., Aaheim, A., Benduhn, F., Lawrence, M., and Timmreck, C.: Solar irradiance
479 reduction to counteract radiative forcing from a quadrupling of CO₂: Climate responses simulated
480 by four earth system models, *Earth Syst. Dynam.*, 3, 63–78, [https://doi.org/10.5194/esd-3-63-](https://doi.org/10.5194/esd-3-63-2012)
481 2012, 2012.

482 Seifritz, W.: Mirrors to halt global warming, *Nature*, 340, 603, <https://doi.org/10.1038/340603a0>, 1989.

483 Séférian, R., Delire, C., Decharme, B., Voldoire, A., David, S. Y. M., Chevallier, M., Saint-Martin, D.,
484 Aumont, O., Calvet, J.-C., Carrer, D., Douville, H., Franchistéguy, L., Joetzjer, E., and Sénési, S.:
485 Development and evaluation of CNRM Earth system model – CNRM-ESM1, *Geosci. Model*
486 *Dev.*, 9, 1423–1453, <https://doi.org/10.5194/gmd-9-1423-2016>, 2016.

487 Sudo, K., Takahashi, M., Kurokawa, J., and Akimoto, H.: CHASER: A global chemical model of the
488 troposphere: 1. Model description, *J. Geophys. Res.*, 107, 4339,
489 <https://doi.org/10.1029/2001JD001113>, 2002.

490 Sun, W., Wang, B., Chen, D., Gao, C., Lu, G., and Liu, J.: Global monsoon response to tropical and
491 Arctic stratospheric aerosol injection, *Clim. Dyn.*, 55, 2107–2121,
492 <https://doi.org/10.1007/s00382-020-05371-7>, 2020.

493 Taylor, K. E.: Summarizing multiple aspects of model performance in a single diagram, *J. Geophys.*
494 *Res.-Atmos.*, 106, 7183–7192, <https://doi.org/10.1029/2000JD900719>, 2001.

495 Taylor, K. E., Stouffer, R. J., and Meehl, G. A.: An overview of CMIP5 and the experiment design,
496 *Bull. Amer. Meteorol. Soc.*, 93, 485–498, <https://doi.org/10.1175/BAMS-D-11-00094.1>, 2012.

497 Tilmes, S., Müller, R., and Salawitch, R.: The sensitivity of polar ozone depletion to proposed
498 geoengineering schemes, *Science*, 320, 1201–1204, <https://doi.org/10.1126/science.1153966>,
499 2008.

500 Tilmes, S., Fasullo, J., Lamarque, J. F., Marsh, D. R., Mills, M., Alterskjær, K., Muri, H., Kristjánsson,
501 J. E., Boucher, O., Schulz, M., Cole, J. N. S., Curry, C. L., Jones, A., Haywood, J., Irvine, P. J.,
502 Ji, D., Moore, J. C., Karam, D. B., Kravitz, B., Rasch, P. J., Singh, B., Yoon, J.-H., Niemeier, U.,
503 Schmidt, H., Robock, A., Yang, S., and Watanabe, S.: The hydrological impact of geoengineering
504 in the Geoengineering Model Intercomparison Project (GeoMIP), *J. Geophys. Res.-Atmos.*, 118,
505 11036–11058, <https://doi.org/10.1002/jgrd.50868>, 2013.

506 Tilmes, S., Richter, J. H., Kravitz, B., MacMartin, D. G., Mills, M. J., Simpson, I. R., Glanville, A. S.,
507 Fasullo, J. T., Phillips, A. S., Lamarque, J.-F., Tribbia, J., Edwards, J., Mickelson, S., and Ghosh,
508 S.: CESM1 (WACCM) stratospheric aerosol geoengineering large ensemble project, *Bull. Amer.*
509 *Meteorol. Soc.*, 99, 2361–2371, <https://doi.org/10.1175/BAMS-D-17-0267.1>, 2018.

510 Tilmes, S., Vioni, D., Jones, A., Haywood, J., Séférian, R., Nabat, P., Boucher, O., Bednarz, E. M.,
511 and Niemeier, U.: Stratospheric ozone response to sulfate aerosol and solar dimming climate
512 interventions based on the G6 Geoengineering Model Intercomparison Project (GeoMIP)
513 simulations, *Atmos. Chem. Phys.*, 22, 4557–4579, <https://doi.org/10.5194/acp-22-4557-2022>,
514 2022.

515 Trenberth, K. E., and Dai, A.: Effects of Mount Pinatubo volcanic eruption on the hydrological cycle
516 as an analog of geoengineering, *Geophys. Res. Lett.*, 34, 1438–1442,
517 <https://doi.org/10.1029/2007GL030524>, 2007.

518 United Nations Environment Programme.: Emissions Gap Report 2020, UNEP, Nairobi, 2020.

519 Vioni, D., Pitari, G., di Genova, G., Tilmes, S., and Cionni, I.: Upper tropospheric ice sensitivity to
520 sulfate geoengineering, *Atmos. Chem. Phys.*, 18, 14867–14887, [https://doi.org/10.5194/acp-18-](https://doi.org/10.5194/acp-18-14867-2018)
521 14867-2018, 2018.

522 Vioni, D., MacMartin, D. G., and Kravitz, B.: Is turning down the sun a good proxy for stratospheric

523 sulfate geoengineering? *J. Geophys. Res.-Atmos.*, 126, e2020JD033952,
524 <https://doi.org/10.1029/2020JD033952>, 2021.

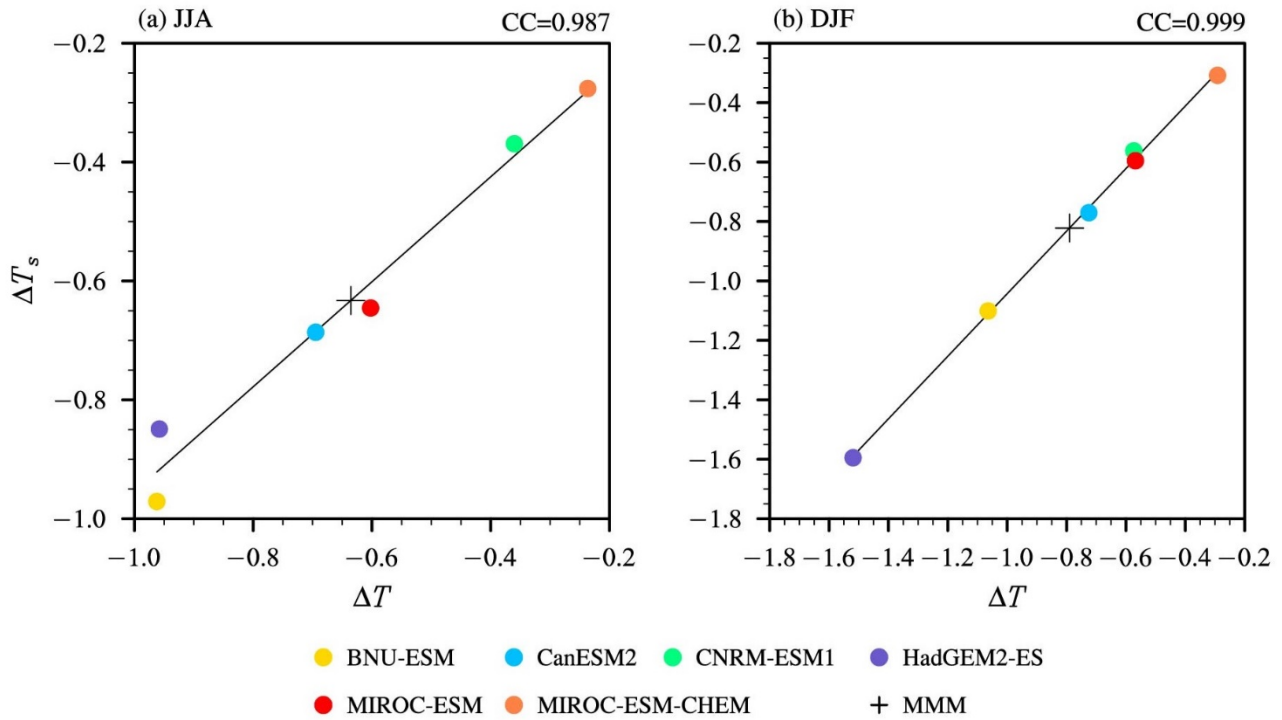
525 Watanabe, S., Hajima, T., Sudo, K., Nagashima, T., Takemura, T., Okajima, H., Nozawa, T., Kawase,
526 H., Abe, M., Yokohata, T., Ise, T., Sato, H., Kato, E., Takata, K., Emori, S., and Kawamiya, M.:
527 MIROC-ESM 2010: Model description and basic results of CMIP5-20c3m experiments, *Geosci.*
528 *Model Dev.*, 4, 845–872, <https://doi.org/10.5194/gmd-4-845-2011>, 2011.

529 Wigley, T. M. L.: A combined mitigation/geoengineering approach to climate stabilization, *Science*,
530 314, 452–454, <https://doi.org/10.1126/science.1131728>, 2006.

531 Wu, J., and Gao, X.: A gridded daily observation dataset over China region and comparison with the
532 other datasets, *Chinese J. Geophys.*, 56, 1102–1111, <https://doi.org/10.6038/cjg20130406>, 2013.
533 (in Chinese)

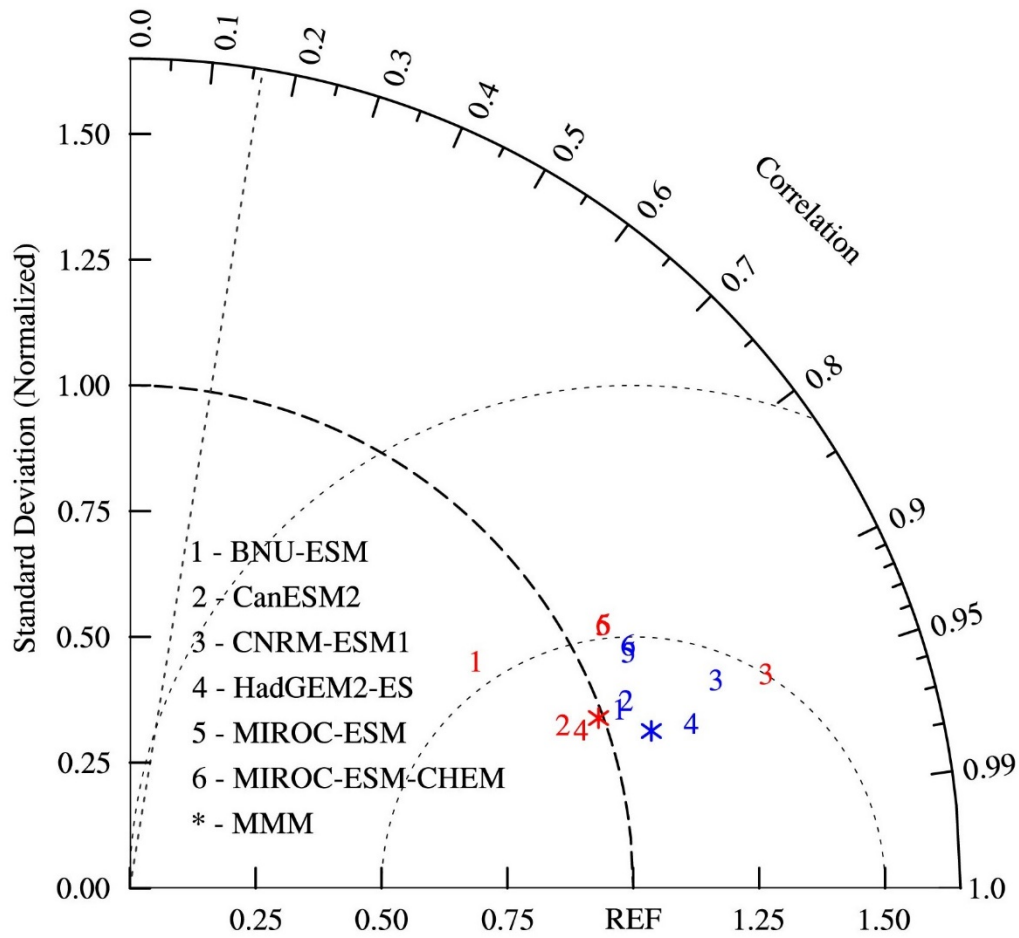
Table 1. Main features of climate models used in this study.

Model	Atmospheric resolution (longitude, latitude, and vertical levels)	Ensemble number	Stratospheric aerosol	Reference
BNU-ESM	$\sim 2.8^\circ \times \sim 2.8^\circ$, L26	1	Prescribed	Ji et al., 2014
CanESM2	$\sim 2.8^\circ \times \sim 2.8^\circ$, L35	3	Uniform	Arora et al., 2011
CNRM-ESM1	$\sim 1.4^\circ \times \sim 1.4^\circ$, L31	2	Prescribed	Séférian et al., 2016
HadGEM2-ES	$1.875^\circ \times 1.25^\circ$, L38	3	Generated from SO ₂ injection	Collins et al., 2011
MIROC-ESM	$\sim 2.8^\circ \times \sim 2.8^\circ$, L80	1	Prescribed	Watanabe et al., 2011
MIROC-ESM-CHEM	$\sim 2.8^\circ \times \sim 2.8^\circ$, L80	1	Prescribed	Watanabe et al., 2011



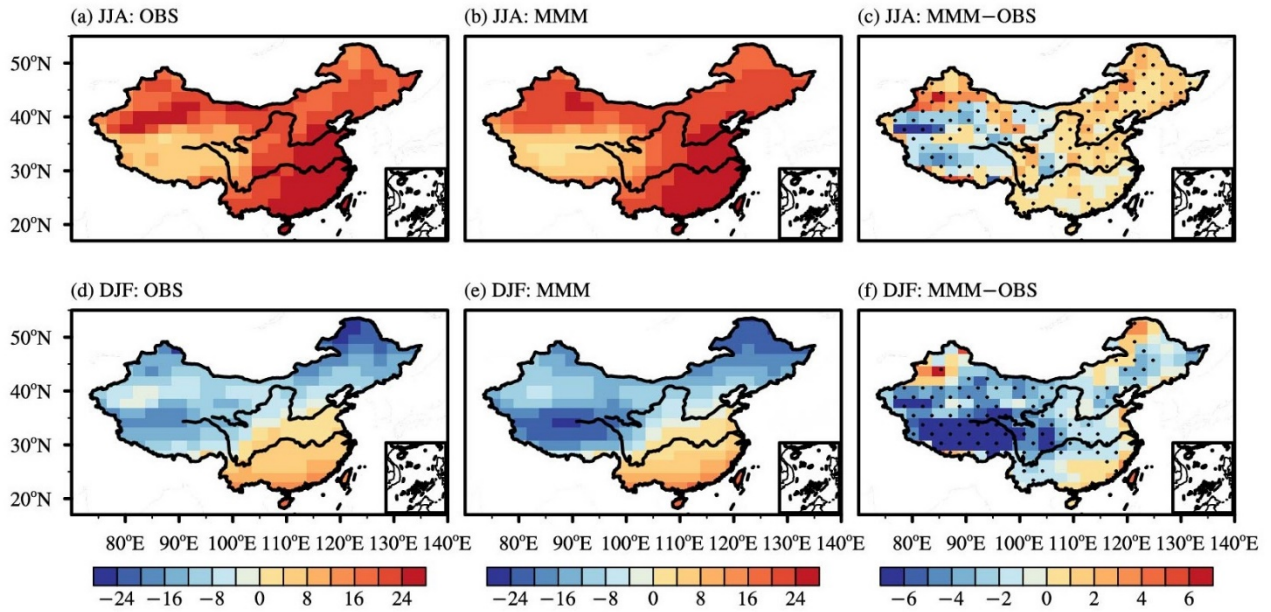
536

537 **Figure 1.** Scatter plots of relationship between changes in surface air temperature (T) and surface
 538 temperature (T_s) over China due to SAI forcing during the period of 2030–2069 in (a) summer (JJA)
 539 and (b) winter (DJF), and CC is their correlation coefficient. Scatters and cross represent individual
 540 models and their mean, respectively.



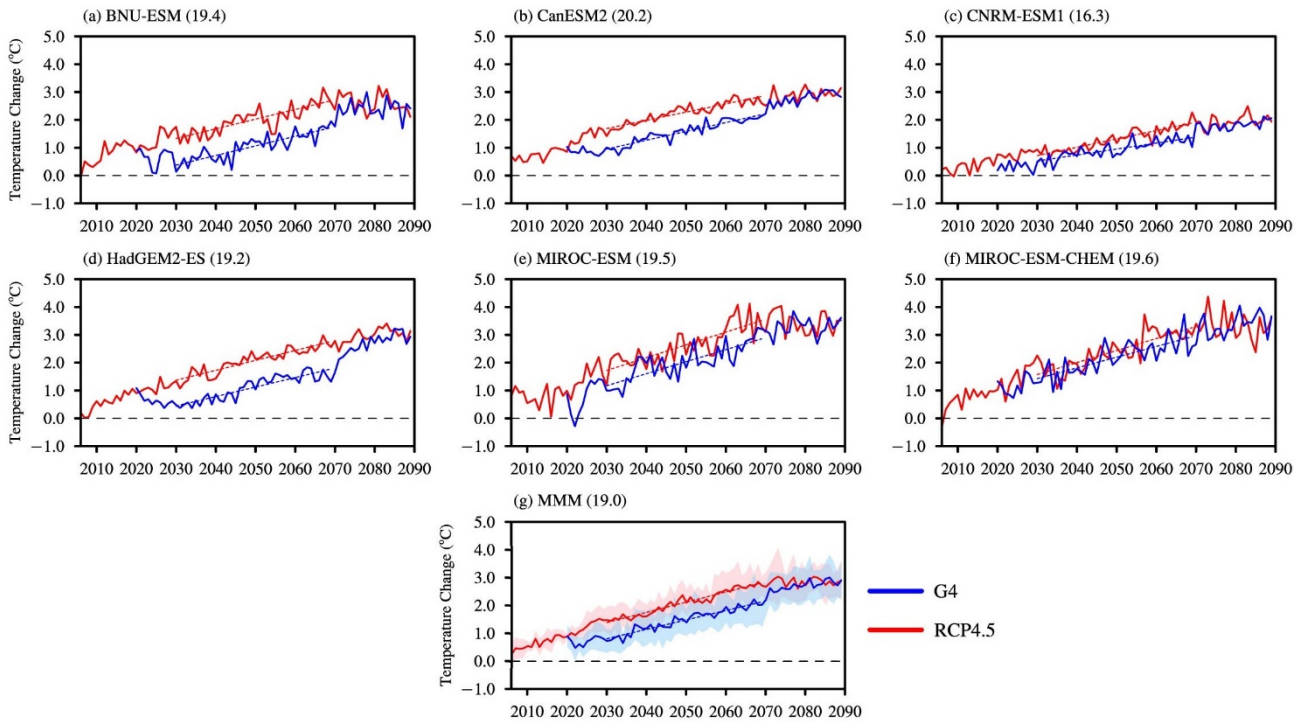
541

542 **Figure 2.** Taylor diagram of climatological summer and winter temperatures over China between the
 543 historical simulations in selected models and observation during the period of 1986–2005. Numbers
 544 represent individual models, and asterisks represent the multi-model mean. Red and blue represent
 545 summer and winter, respectively. The dotted straight line shows the 99% confidence level determined
 546 from the two-tailed Student’s *t*-test.



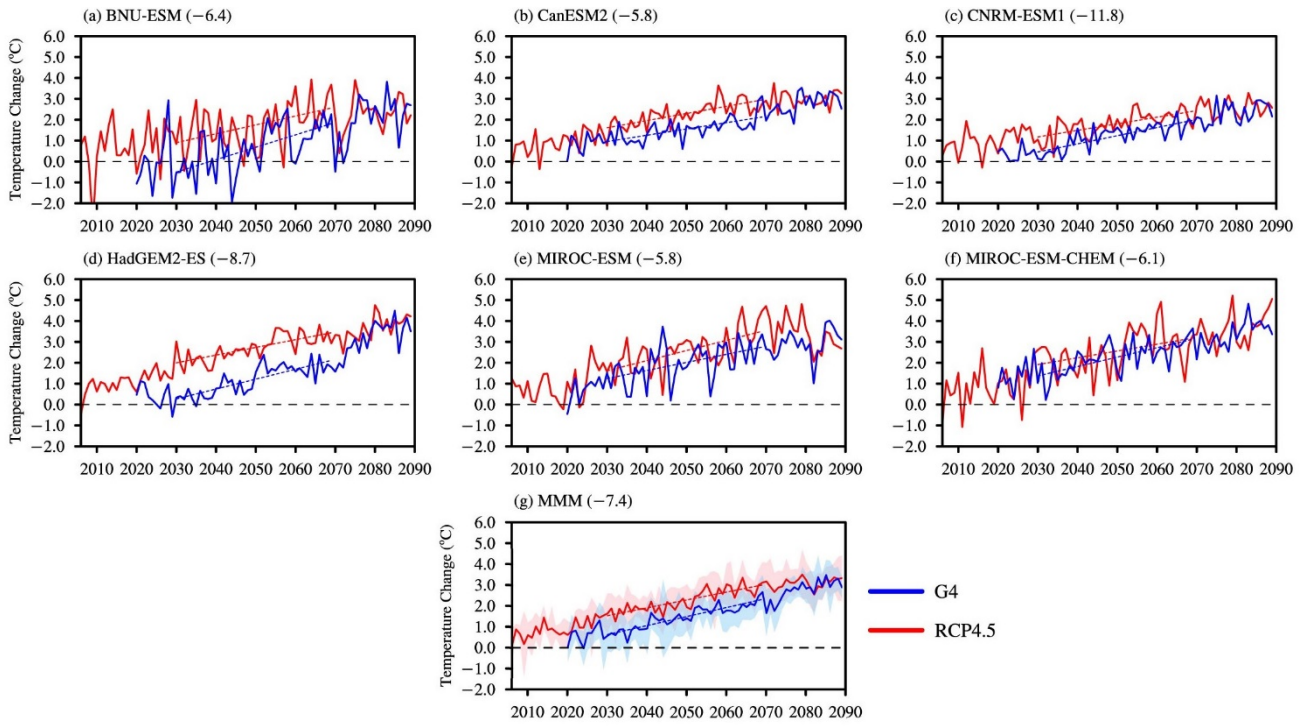
547

548 **Figure 3.** Spatial patterns of surface air temperature climatology (units: °C) over China as obtained
 549 from observation (left column; OBS), the multi-model mean (middle column; MMM), and the
 550 difference between multi-model mean and observation (right column; MMM-OBS) during the period
 551 of 1986–2005 in summer (JJA) and winter (DJF). The dots in the right column indicate areas where at
 552 least two-thirds of models share the same sign of the bias.



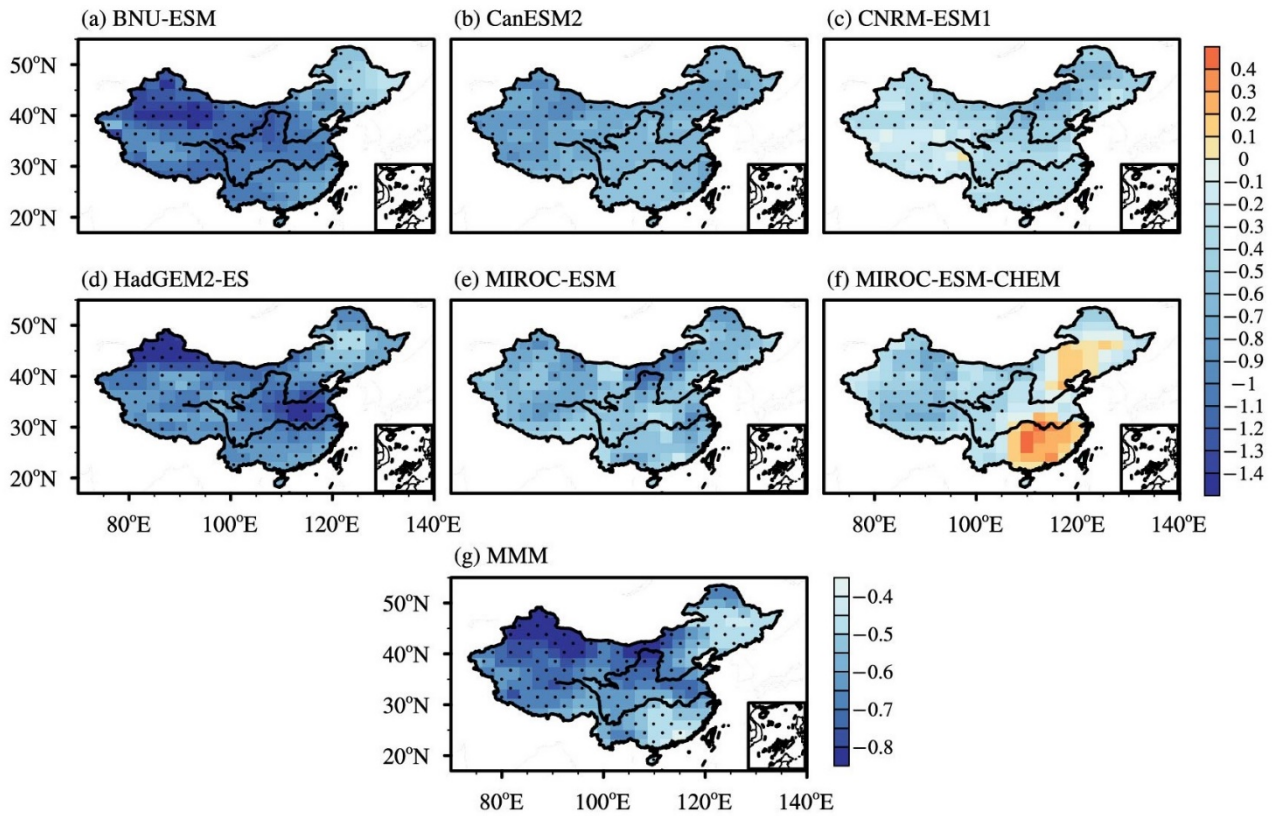
553

554 **Figure 4.** Time series of regionally averaged surface air temperature (units: °C) over China in the G4
 555 experiment (solid blue lines) and RCP4.5 scenario (solid red lines) in summer. The values are obtained
 556 by subtracting the present climatology (mean of 1986–2005; represented in parentheses) in the
 557 historical experiment. Red and blue dashed lines represent the linear trends of G4 and RCP4.5
 558 simulations during the period of 2030–2069, respectively. The multi-model mean (MMM) is
 559 represented at the bottom, with the shading indicating one inter-model standard deviation.



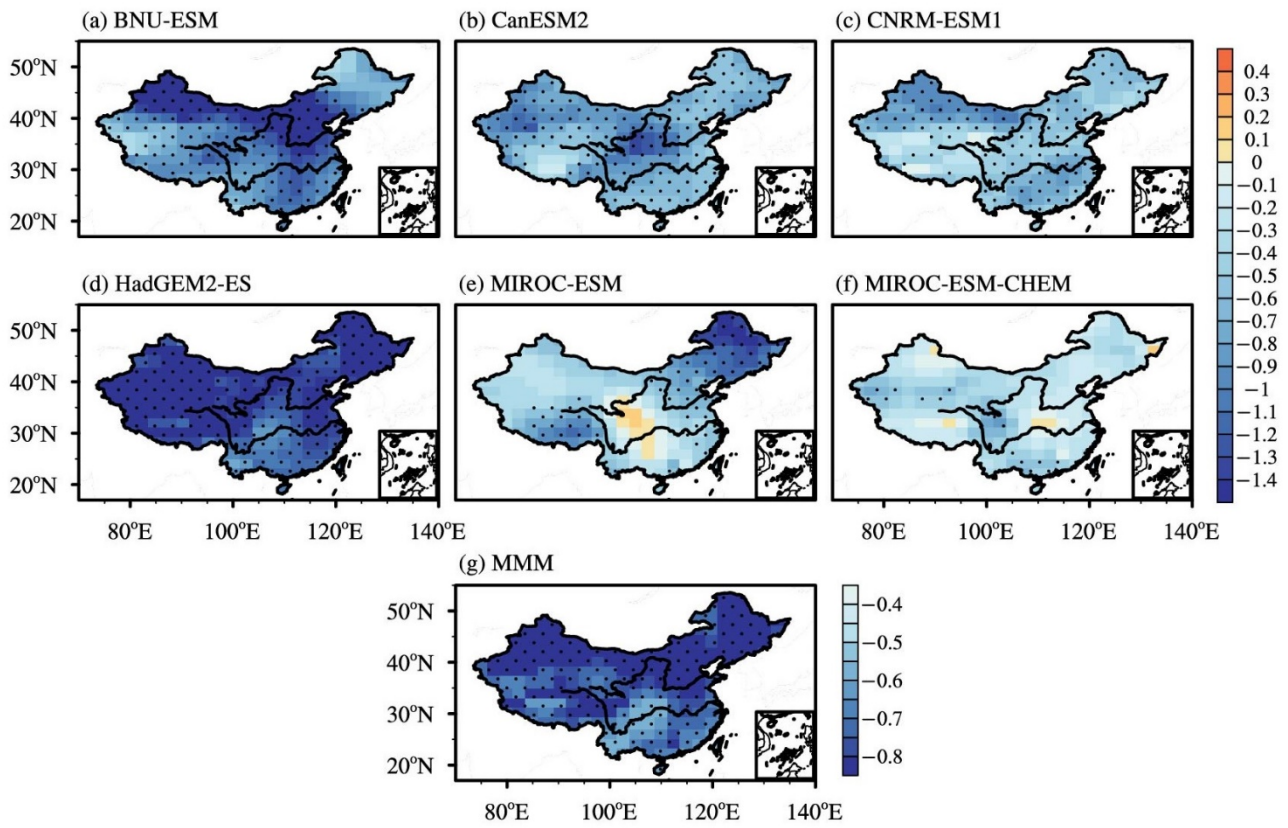
560

561 **Figure 5.** Same as Figure 4, but in winter.



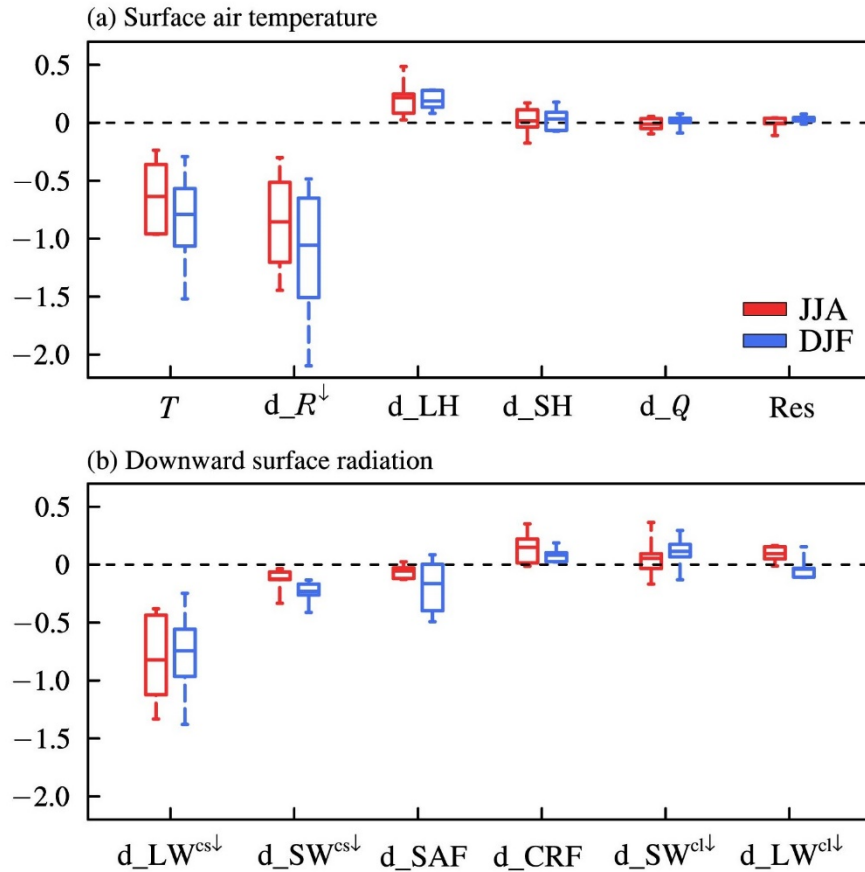
562

563 **Figure 6.** Spatial patterns of surface air temperature differences (units: °C) between G4 and RCP4.5
 564 over China during the period of 2030–2069 in summer for (a–f) individual models and (g) the multi-
 565 model mean. The dots in (a–f) indicate areas where are statistically significant at the 90% confidence
 566 level. The dots in (g) indicate areas where at least two-thirds of models share the same sign with the
 567 multi-model mean.



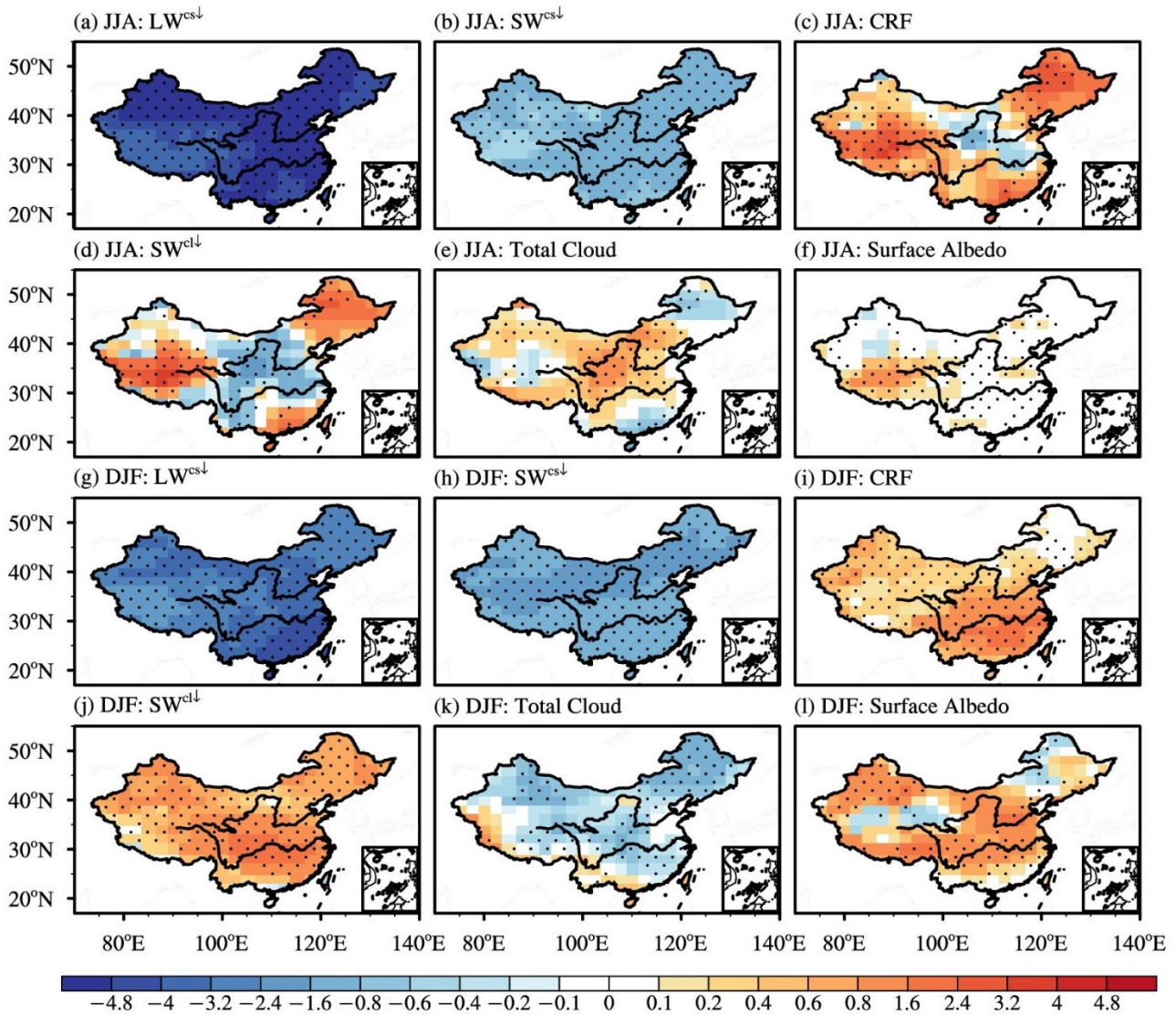
568

569 **Figure 7.** Same as Figure 6, but in winter.



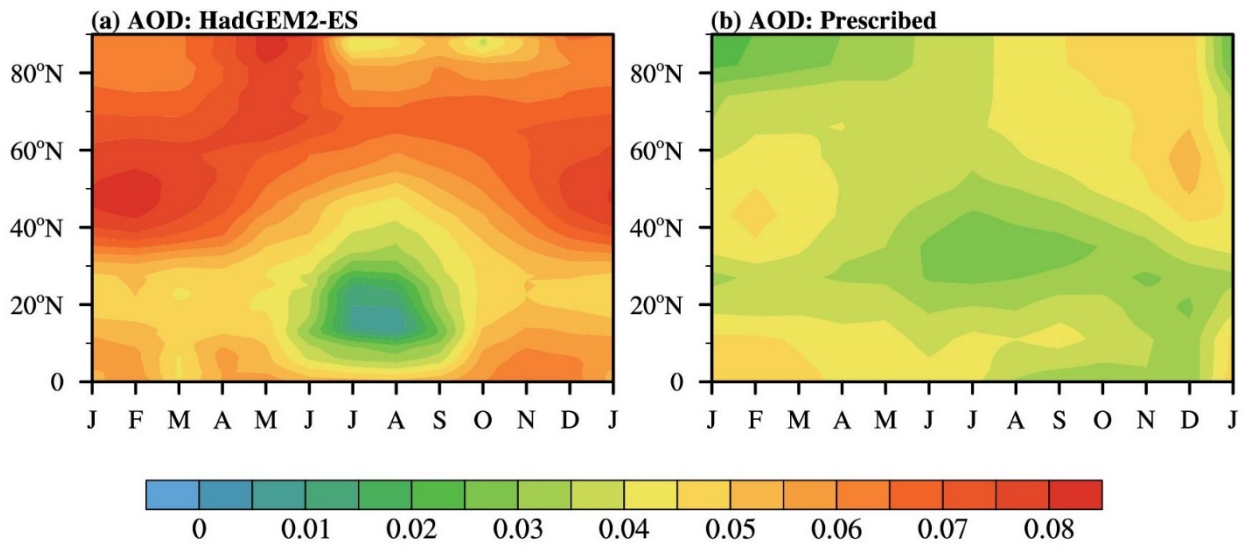
570

571 **Figure 8.** Regionally averaged SAI-induced changes in surface air temperature (T) and relevant terms
 572 over China during the period of 2030–2069 (units: $^{\circ}\text{C}$). The terms include surface air temperature
 573 changes due to (a) downward net surface radiation change ($d_{R^{\downarrow}}$), surface latent (d_{LH}) and sensible
 574 (d_{SH}) heat flux changes, heat storage change (d_Q), residual term change (Res), (b) downward clear-
 575 sky surface longwave ($d_{LW}^{cs\downarrow}$) and shortwave ($d_{SW}^{cs\downarrow}$) radiation changes, surface albedo feedback
 576 change (d_{SAF}) and surface cloud radiative forcing change (d_{CRF} ; including shortwave ($d_{SW}^{cl\downarrow}$)
 577 and longwave ($d_{LW}^{cl\downarrow}$) forcing changes). The error bars represent minimum and maximum values,
 578 and the boxes represent interquartile ranges among models. The middle lines present multi-model
 579 means. The red and blue bars represent values in summer and winter, respectively.



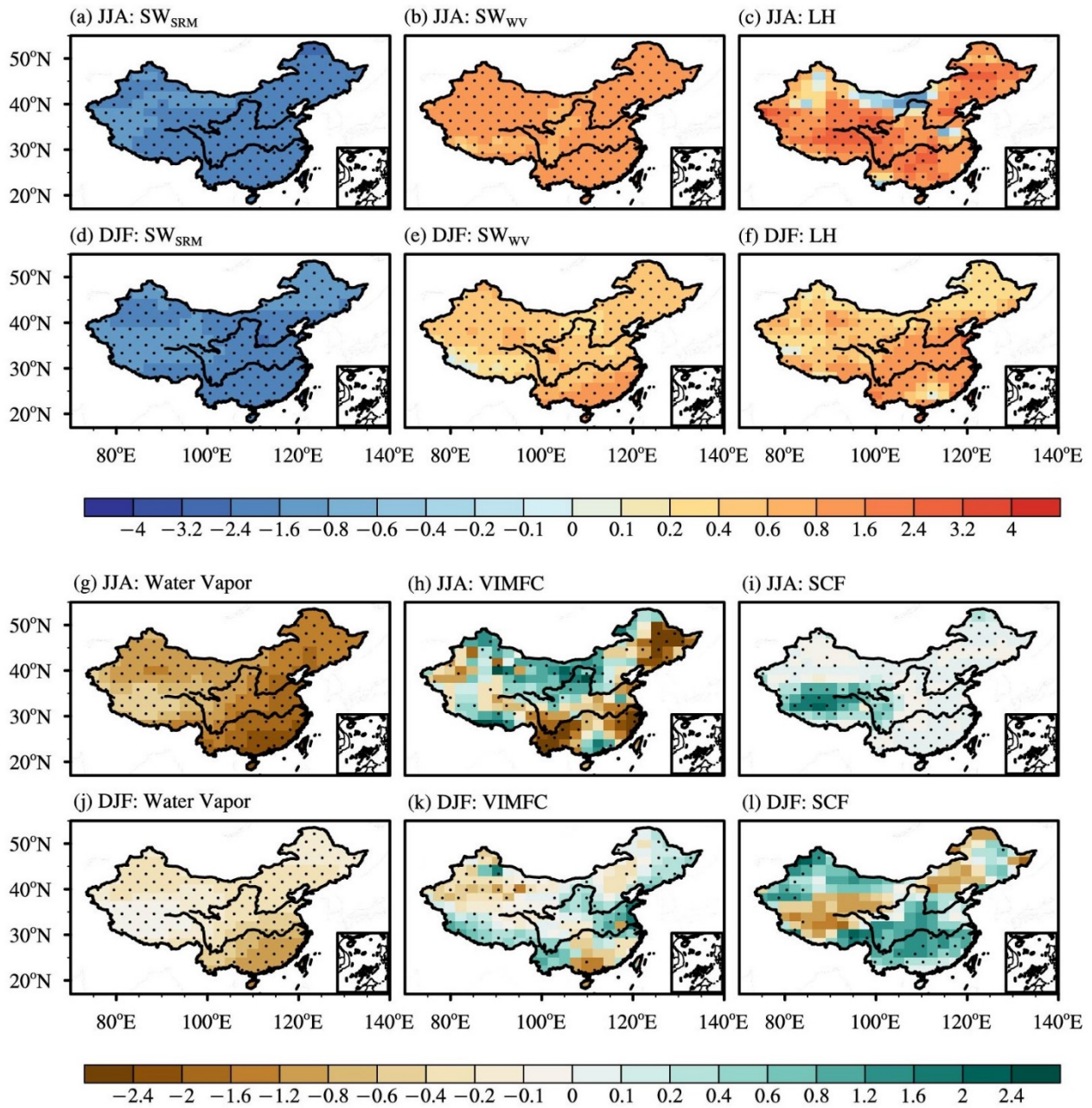
580

581 **Figure 9.** Spatial patterns of differences between G4 and RCP4.5 over China for the multi-model mean
 582 in summer (JJA) and winter (DJF): (a, g) downward clear-sky surface longwave radiation ($LW^{cs\downarrow}$); (b,
 583 h) downward clear-sky surface shortwave radiation ($SW^{cs\downarrow}$); (c, i) surface cloud radiative forcing; (d,
 584 j) downward shortwave radiative effect of clouds ($SW^{cl\downarrow}$); (e, k) total cloud cover (units: %); (f, l)
 585 surface albedo (units: %) during the period of 2030–2069. Flux is in $W\ m^{-2}$. The dots indicate areas
 586 where at least two-thirds of models share the same sign with the multi-model mean.



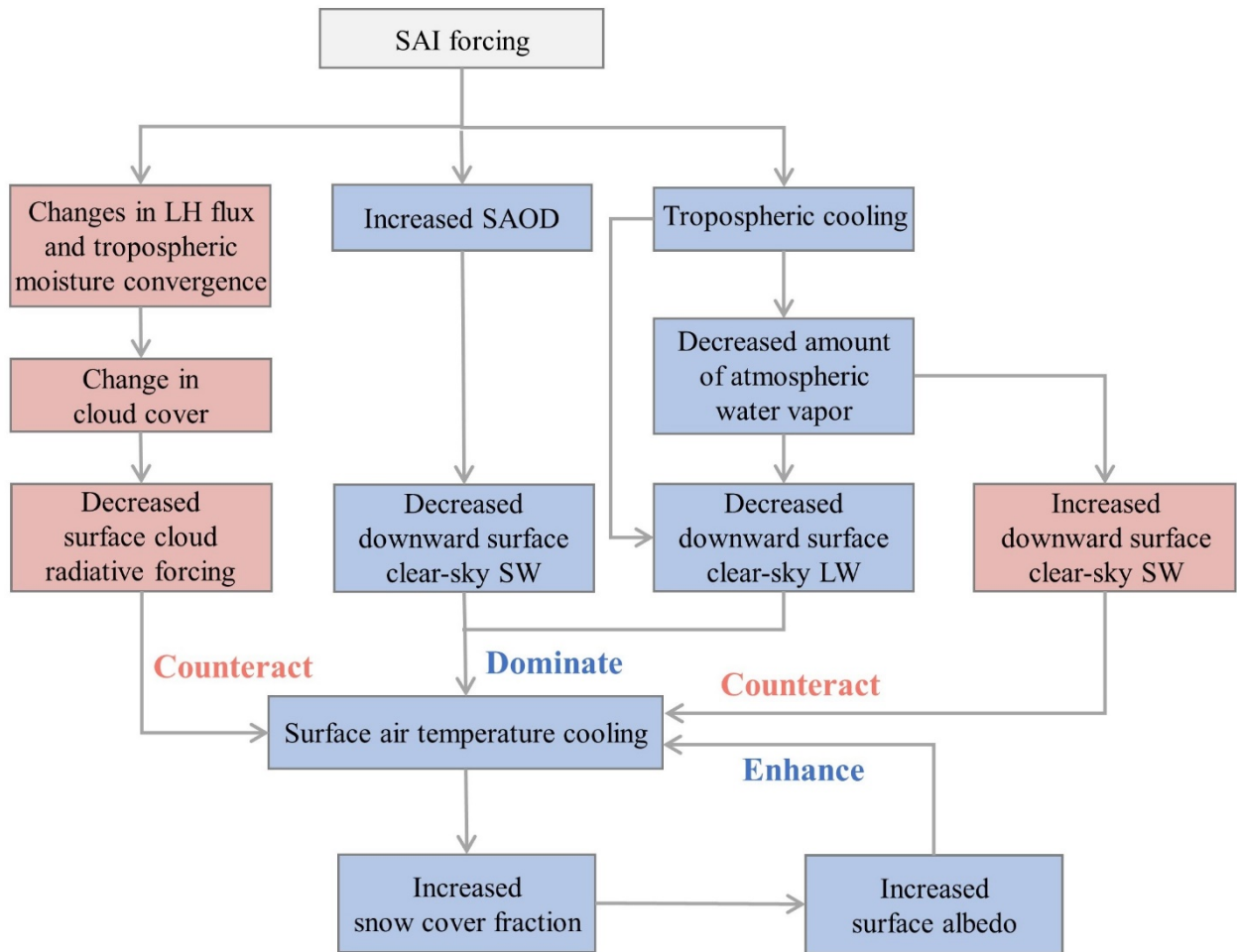
587

588 **Figure 10.** Latitudinal distributions of the calculated (a, for HadGEM2-ES) and prescribed (b, for
 589 BNU-ESM, CNRM-ESM1, and the MIROC-based models) changes in SAOD at 550 nm caused by
 590 SAI in G4 experiment over the Northern Hemisphere during the period of 2030–2069.



591

592 **Figure 11.** Same as Figure 9, but for the shortwave radiative effects of (a, d) solar radiation scattering
 593 change (SW_{SRM}) and (b, e) atmospheric water vapor amount change (SW_{WV}), (c, f) latent heat flux
 594 (LH), (g, j) column-integrated water vapor (units: kg m^{-2}), (h, k) vertically integrated moisture flux
 595 convergence (VIMFC; units: 0.1 mm d^{-1}), and (i, l) snow cover fraction (SCF; units: %). Flux is in W
 596 m^{-2} and defined positive downward.



597

598 **Figure 12.** Schematic diagram illustrating how the relevant physical processes impact the downward

599 surface radiation changes over China in response to the SAI forcing in the G4 experiment.